*Proceedings of the 21st ICSMGE, Vienna, Austria, 14 – 19 June 2026. Pistrol, Adam & Schweiger (eds.)*
*Published by: ÖGG, Austrian Society for Geomechanics, Salzburg, Austria, ISBN 978-3-9503898-4-5*
*https://doi.org/10.53243/ICSMGE2026-645*

# Aperture size effects on the behavior of geogrid-stabilized aggregates under constant radial stiffness triaxial test

**Ziheng Wang**, Jianfeng Xue, Yue Chen
*School of Engineering and Technology, The University of New South Wales, Canberra, Australia, jianfeng.xue@unsw.edu.au*

Amir Shahkolahi
*Global Synthetics Pty Ltd, Brisbane, Australia*

Mark B. Jaksa
*School of Architecture and Civil Engineering, University of Adelaide, Adelaide, Australia*

Chaminda Gallage
*School of Civil and Environmental Engineering, Queensland University of Technology, Brisbane, Australia*

ABSTRACT: Geogrids are widely utilized in unbound base layers to mitigate permanent deformation by providing lateral restraint. This study investigates the impact of geogrid aperture size on the performance of geogrid-stabilized unbound granular materials (UGMs) through a series of Constant Radial Stiffness Triaxial (CRST) tests. Four types of 3D printed geogrids, with aperture counts of 4, 9, 16, and 36, respectively, were fabricated to comparable stiffness. The results demonstrate that geogrid stabilization significantly reduces permanent deformation by enhancing confining stress, especially within the first 3,000 loading cycles. The findings highlight the critical role of the aperture size to $D_{50}$ ratio in minimizing permanent deformation and improving confinement in UGMs. The most effective performance corresponds to $A/D_{max}$, $A/D_{90}$, and $A/D_{50}$ ratios of 1.32, 1.89, and 5.15, respectively, under the test conditions. Aperture sizes either larger or smaller than this optimal ratio result in reduced stabilization effectiveness. Moreover, this study offers valuable insights into residual stress development and shakedown behavior under the CRST condition, underscoring the utility of CRST tests in quantifying the impact of geogrids on UGMs under cyclic loading.

KEYWORDS: Size effects, constant radial stiffness triaxial tests, 3D printed geogrid, aggregate stabilization.

## 1 INTRODUCTION

Pavement engineers face significant challenges when designing and constructing flexible pavements on weak subgrade soils (Berg 2000; Tang et al. 2016). The subgrade acts as the foundation of pavement structures, and pavements built on weak subgrades often exhibit excessive surface rutting. To address this issue, engineers typically use thicker base layers to reduce rutting. However, this approach increases the demand for natural aggregates, which can lead to environmental concerns and higher construction costs (Zadehmohamad et al. 2022). As an alternative, incorporating geosynthetics has proven effective in improving the overall performance of flexible pavements, extending their service life, reducing costs, and addressing environmental issues (Al-Qadi et al. 1994; Han et al. 2011). Geosynthetics are commercially available in various forms and materials, among which geogrids are widely used in unbound base layers. Composed of longitudinal and transverse ribs, geogrids confine aggregates and restrict their lateral movement, thereby enhancing the structural performance of pavement systems (Giroud and Han 2004).

Numerous laboratory tests have been conducted to investigate the mechanisms governing geogrid–aggregate interaction, employing various testing methods such as the plate load test (PLT), direct shear test (DST), repeated load triaxial test (RLTT), and pullout test. However, the geogrid–aggregate interaction is complex and influenced by multiple factors, including the properties of the aggregate and geogrid, the aperture-to-particle size ratio ($A/D_{50}$), and the loading conditions. Tavakoli and Khazaei (2017) performed a series of cyclic PLTs and reported that the optimal nominal aperture size of geogrids should be approximately four times the median grain size of the soil. Han et al. (2018) conducted large-scale DSTs to evaluate the shear behavior at the aggregate–geogrid interface and found that effective interlock was achieved when the aperture-to-particle size ratio ($A/D_{50}$) ranged from 1.30–1.71 for biaxial geogrids and 1.08–1.43 for triaxial geogrids. Similarly, Oliveira and Falorca (2025), based on RLTTs, highlighted improved mechanical performance when the ratio between the geogrid aperture size and the median particle diameter approached unity.

Although several studies have attempted to determine the optimum ratio of geogrid aperture size to aggregate particle size, their conclusions often differ or even contradict each other due to variations in test methods and conditions. Each testing method has inherent limitations. For instance, large-scale cyclic plate load tests are time-consuming and costly as they require substantial soil tank sizes, leading to considerable preparation time, material consumption, and labor (Sun et al. 2015). Moreover, the stress conditions applied to aggregates in DST and pullout tests differ significantly from those encountered in the field, potentially limiting their applicability. Even the RLTT, despite its widespread application, may not fully capture field-relevant stress conditions. Specifically, the RLTT under constant confining stress typically employs a stress path with a horizontal-to-vertical stress ratio of 1:3, whereas pavement layers in service are subjected to stress ratios ranging from 1:1.1 to 1:2.4 (Dutta and Kodikara 2022).

To overcome the limitations of conventional methods, this study adopts a novel approach using the Precision Unbound Material Analyzer (PUMA), a laboratory device that operates under the constant radial stiffness triaxial (CRST) boundary condition. This apparatus has been employed in several studies and offers notable advantages over the RLTT (Li et al. 2020; Kodikara et al. 2024). Unlike the RLTT, PUMA utilizes a dynamically varying confining stress that better replicates the influence of surrounding materials in pavement structures under traffic loading (Sun et al. 2020). Moreover, while the conventional RLTT predominantly induce shear-dominated responses in unbound granular materials, rutting in pavements is largely driven by excessive plastic compression accompanied by lateral spreading. The CRST boundary condition employed by the PUMA device effectively captures these stress states, thereby providing a more accurate representation of in-service pavement behavior. Recent findings by the authors (Wang et al., 2025) further support the effectiveness of this method, demonstrating that geogrid-stabilized aggregates exhibit significantly reduced permanent deformation under the CRST condition. This improvement is attributed to the enhanced lateral confinement provided by the geogrid, clearly highlighting the interlocking mechanism between the geogrid and aggregate particles. However, only one type of geogrid with a unique aperture size was used in the tests.

In this study, a series of CRST tests were performed using the PUMA to investigate the influence of geogrid aperture size on the performance of geogrid-stabilized unbound granular materials (UGMs) under cyclic loading.

## 2 METHODOLOGY

### 2.1 *Unbound granular materials*

The material used in this study is crushed blue metal, which is typically used for constructing the base layer for flexible pavements in Australia. Two standard geotechnical tests, sieve analysis (ASTM C136) and the modified Proctor compaction test (ASTM D1557), were conducted to determine its properties. The particle size distribution is shown in Figure 1, and the material properties are summarized in Table 1.

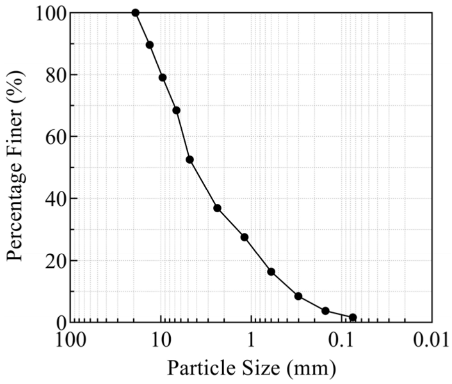


Figure 1. Particle size distribution of the test material.

Table 1. Material properties of crushed blue metal.

| Material property | Value |
|---|---|
| USCS classification | GW |
| $D_{max}$ (mm) | 19.0 |
| $D_{90}$ (mm) | 13.2 |
| $D_{50}$ (mm) | 4.85 |
| Cu | 16.04 |
| Cc | 1.26 |
| Optimum moisture content (%) | 7.04 |
| Maximum dry density (kg/m$^3$) | 2,178 |

### 2.2 *3D printed geogrids*

The additive-manufactured geogrids were fabricated from polyethylene terephthalate glycol (PETG). As shown in Figure 2, four geogrid configurations were designed using CAD software, featuring aperture counts of 4, 9, 16, and 36 to fit within the 150 mm diameter PUMA mold. The corresponding aperture sizes were 36.9, 25.0, 18.5, and 12.6 mm. The geogrids were fabricated at predetermined scaling ratios, enabling adjustments to aperture size and rib width while maintaining similar tensile strength across all models. The ratios of geogrid aperture size to particle sizes, including $D_{max}$, $D_{90}$, and $D_{50}$, are presented in Table 2.

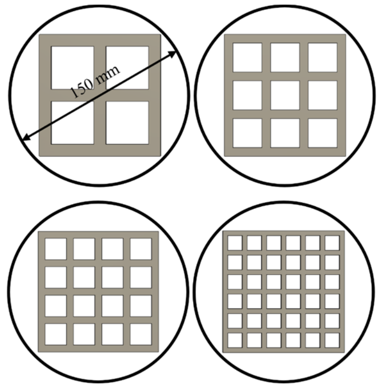


Figure 2. Four types of 3D printed geogrids.

Table 2. The ratio of geogrid aperture size to particle size (A/D).

| Geogrid | Aperture size (mm) | $A/D_{max}$ | $A/D_{90}$ | $A/D_{50}$ |
|---|---|---|---|---|
| T36.9 | 36.9 | 1.94 | 2.80 | 7.61 |
| T25.0 | 25.0 | 1.32 | 1.89 | 5.15 |
| T18.5 | 18.5 | 0.97 | 1.40 | 3.81 |
| T12.6 | 12.6 | 0.66 | 0.95 | 2.60 |

### 2.3 *Test Procedures*

Figure 3 illustrates the PUMA setup. The device features a split mold confined by a rubber-lined steel band. The specimen mold, with internal dimensions of 150 mm in height and 150 mm in diameter, is constructed from eight curved wall segments. These wall segments are connected by H-shaped connectors, allowing for lateral expansion of the specimen. The rubber-lined steel band consists of a 10 mm thick rubber band and a 0.26 mm thick steel band. The rubber band provides constant stiffness, simulating the elastic confinement of the surrounding in-situ material. A full-bridge strain gauge is installed at the center height of the steel band to measure strain when the specimen undergoes lateral deformation. Additionally, a pair of high-precision linear variable differential transducers (LVDTs) are attached to the top cap at diametrically opposite ends to record the vertical deformation of the specimen.

The oven-dried soil was first mixed with water to achieve an optimum moisture content of 7.04%, then stored in airtight containers for at least 24 hours to ensure uniform water distribution. The soil was then compacted in the PUMA mold in five layers to within ±1% of the maximum dry density using a modified Proctor compactor. For the stabilized specimens, the geogrid was positioned at the middle height of the specimen. It was placed after the first half of the material in the third layer was poured, followed by the addition of the remaining material. Compaction of the third layer was then completed. During specimen preparation, two compaction jacket sections were tightly locked to initially restrain the side walls. After compaction, the confining band was placed at the middle height of the mold, and the compaction jackets were carefully removed. An initial confining stress ($\sigma_{3,i}$) of approximately 10 kPa was then applied to the specimens.

To investigate the influence of geogrid aperture size on the performance of geogrid-stabilized UGMs under cyclic loading, four specimens stabilized with 3D printed geogrids, designated as T36.9, T25.0, T18.5, and T12.6 as per their aperture sizes, were tested. These specimens were subjected to 10,000 cycles of repeated loading. The loading waveform consisted of a haversine pulse with a 0.1-second loading phase and a 0.9-

second rest period, in accordance with the AASHTO T307 specification. The cyclic vertical stress applied to the specimens was 300 kPa. A detailed vertical stress correction method addressing the effect of wall friction in the PUMA cell is provided in Wang et al. (2025). This stress level is sufficient to capture the common stress level received at the base layer or high stress level received at the subbase layer. The accumulated plastic and resilient strains for each cycle in both vertical and horizontal directions were recorded using axial LVDTs and radial strain gauges, respectively.

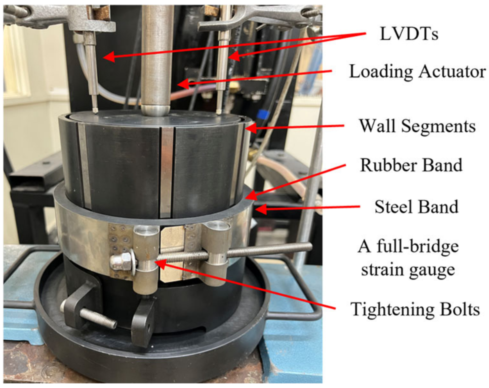

Figure 3. PUMA device setup.

## 3 RESULTS

### 3.1 *Axial permanent strain*

Figure 4 illustrates the accumulation of axial permanent strain ($\varepsilon_{1,p}$) with the number of loading cycles for all specimens. The permanent deformation response can be divided into two distinct phases. In the initial phase, a rapid increase in permanent deformation is observed, corresponding to the post-compaction compression stage as described in shakedown theory. This behavior is primarily attributed to particle reorientation and lateral spreading. Notably, the majority of the stabilization benefits offered by the geogrid occur within the first 3,000 loading cycles, underscoring the significance of confinement effects that limit the lateral movement of aggregate particles. Among the geogrid-stabilized specimens, T25.0 (with an aperture size of 25.0 mm) exhibited the greatest reduction in permanent strain, followed by T36.9, T18.5, and T12.6. The second phase, referred to as the secondary cyclic compression stage, is characterized by a substantially reduced rate of permanent strain accumulation, where deformation predominantly arises from particle contact degradation. During this stage, specimens T25.0 and T36.9, along with the unstabilized control specimen, exhibited relatively stable responses, characterized by comparable permanent strain rates. In contrast, specimens stabilized with T12.6 and T18.5 showed slight fluctuations, potentially due to minor slippage at the geogrid–aggregate interface, likely influenced by the smaller aperture sizes.

### 3.2 *Radial confining stress*

Lateral spreading is a critical contributor to the permanent deformation of base layers, as evidenced by field observations. In the CRST test, lateral spreading is evaluated by monitoring variations in the confining stress($\sigma_3$). The minimum confining stress ($\sigma_{3,min}$) represents the residual confining stress under unloading conditions and progressively accumulates during cyclic loading. Figure 5 depicts the evolution of $\sigma_{3,min}$ with the number of loading cycles for all specimens. Consistent with the trend observed in the development of permanent strain, the $\sigma_{3,min}$ curves also exhibit two distinct phases. Beginning from an initial confining stress of 10 kPa, $\sigma_{3,min}$ increases rapidly within the first 3,000 cycles, after which it enters a relatively steady phase. By the end of the test, all geogrid-stabilized specimens display consistently lower $\sigma_{3,min}$ values than the unstabilized control specimen, indicating improved resistance to lateral spreading. Similar to the results of permanent strain, among the stabilized specimens, T25.0 (25.0 mm aperture) shows the most effective reduction in lateral spreading, followed by T36.9, T18.5, and T12.6.

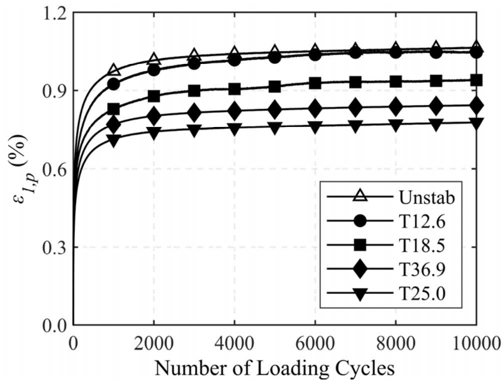

Figure 4. The variation of $\varepsilon_{1,p}$ with the number of loading cycles.

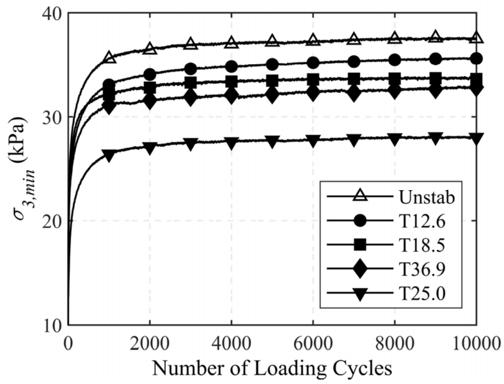

Figure 5. The variation of $\sigma_{3,min}$ with the number of loading cycles.

## 4 DISCUSSION

As shown in Figure 4 and 5, both $\varepsilon_{1,p}$ and $\sigma_{3,min}$ exhibit similar trends across all specimens, suggesting that the observed reduction in $\varepsilon_{1,p}$ can be attributed to the presence of geogrid stabilization. To further illustrate the underlying mechanism, Figure 6 presents schematic diagrams of both unstabilized and geogrid-stabilized specimens. As illustrated in Figure 6(a), all specimens begin from an identical initial condition. Upon application of vertical compression through axial loading, as shown in Figure 6(b), the specimens experience radial expansion. In the stabilized specimens, the geogrid increases the confining effect by restricting lateral displacement of aggregate particles through mechanical interlock. This results in reduced lateral deformation and a lower build-up of confining stress relative to the unstabilized specimen. Under cyclic loading, this process is repeated in each loading cycle, leading to progressive accumulation of both axial permanent strain and confining stress.

Unlike in RLTTs, where the confining stress is externally controlled, the confining stress in CRST tests arises as a reactive stress governed by the boundary conditions. In PUMA tests, geogrid-stabilized specimens exhibit lower confining stress levels, reflecting enhanced radial stiffness. The effectiveness of stabilization is strongly influenced by the interaction at the geogrid–aggregate interface. Figure 7 presents the relationship between $\sigma_{3,min}$ and $\varepsilon_{1,p}$ at the end of the test. A strong linear correlation is observed, providing further evidence that the reduction in permanent axial strain can be attributed to the inclusion of geogrid stabilization. The specimen T25.0 exhibited the most effective performance, with corresponding $A/D_{max}$, $A/D_{90}$, and $A/D_{50}$ ratios of 1.32, 1.89, and 5.15, respectively. Aperture sizes, either larger or smaller than this optimal ratio, result in reduced stabilization effectiveness, which has been reflected in the greater $\sigma_{3,min}$ in the figure as a result of greater lateral deformation.

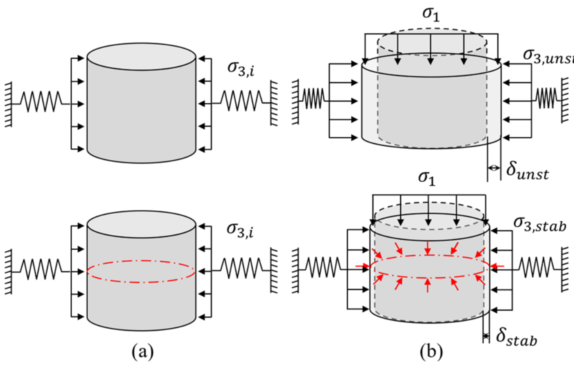

Figure 6. Illustration of geogrid mechanism in PUMA tests.

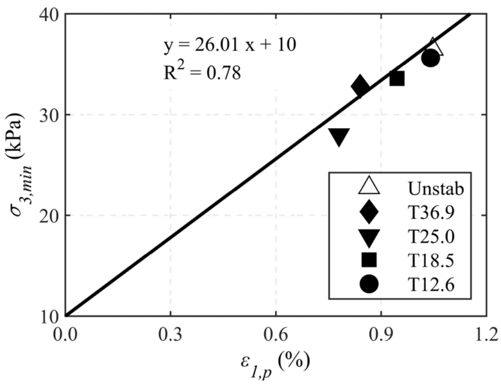

Figure 7. Relationship between $\sigma_{3,min}$ and $\varepsilon_{1,p}$ at the end of the test.

## 5 CONCLUSION

This study investigated the permanent deformation behavior of unbound granular materials (UGMs) with and without geogrid stabilization under cyclic loading using PUMA, a constant radial stiffness triaxial (CRST) test device. The CRST test provides valuable insights into the development of residual stress in pavement materials and their associated shakedown behavior. The results indicate that geogrid stabilization substantially mitigates permanent deformation in UGMs by enhancing lateral confinement. The degree of confinement is influenced by the ratio of geogrid aperture size to particle size, with different ratios affecting the stabilization performance. Further investigations, including numerical simulations and field testing, are planned to validate these laboratory findings and to better understand and quantify the influence of geogrid stabilization in real-world pavement applications.

## 6 ACKNOWLEDGEMENTS

The research is funded by the Australian Research Council (ARC) through an ARC Linkage project LP220100186. Funding received from the following industry partners is also acknowledged: NACOE, Global Synthetics, FSG Geotechnics & Foundations, and Fortify Geotech.

## 7 REFERENCES

Al-Qadi, I.L., Brandon, T.L., Valentine, R.J., Lacina, B.A. and Smith, T.E. 1994. Laboratory evaluation of geosynthetic-reinforced pavement sections. *Transportation research record* (1439), pp. 25–31.

Berg, R.R. 2000. Geosynthetic Reinforcement of the Aggregate Base/Subbase Courses of Pavement Structures.

Duncan-Williams, E. and Attoh-Okine, N.O. 2008. Effect of geogrid in granular base strength–An experimental investigation. *Construction and building materials* 22(11), pp. 2180–2184.

Dutta, T.T. and Kodikara, J. 2022. Evaluation of unbound/subgrade material rutting and resilient behaviour based on initial density and saturation degree. *Transportation Geotechnics* 35, p. 100782. doi: 10.1016/j.trgeo.2022.100782.

Giroud, J.P. and Han, J. 2004. Design method for geogrid-reinforced unpaved roads. II. Calibration and applications. *Journal of Geotechnical and Geoenvironmental Engineering* 130(8), pp. 787–797.

Han, B., Ling, J., Shu, X., Gong, H. and Huang, B. 2018. Laboratory investigation of particle size effects on the shear behavior of aggregate-geogrid interface. *Construction and Building Materials* 158, pp. 1015–1025. doi: 10.1016/j.conbuildmat.2017.10.045.

Han, J., Zhang, Y. and Parsons, R.L. 2011. Quantifying the influence of geosynthetics on performance of reinforced granular bases in laboratory. *Geotechnical Engineering Journal of the SEAGS & AGSSEA* 42(1), pp. 74–83.

Hufenus, R., Rueegger, R., Banjac, R., Mayor, P., Springman, S.M. and Brönnimann, R. 2006. Full-scale field tests on geosynthetic reinforced unpaved roads on soft subgrade. *Geotextiles and geomembranes* 24(1), pp. 21–37.

Kodikara, J., Southararajah, A. and Chen, L. 2024. Reimagining unbound road pavement technology: Integrating testing, design, construction and performance in the post-digital era. *Transportation Geotechnics* 47, p. 101274. doi: 10.1016/j.trgeo.2024.101274.

Li, N., Wang, X., Qiao, R., Ma, B., Shao, Z., Sun, W. and Wang, H. 2020. A prediction model of permanent strain of unbound gravel materials based on performance of single-size gravels under repeated loads. *Construction and Building Materials* 246, p. 118492. doi: 10.1016/j.conbuildmat.2020.118492.

Oliveira, G.M. and Falorca, I.M.C.F.G. 2025. Evaluation of two-layered soils reinforced with 3D printed geogrid models under axisymmetric loading conditions. *Geotextiles and Geomembranes* 53(3), pp. 798–810. doi: 10.1016/j.geotexmem.2025.01.008.

Sun, Q., Dong, Q., Cai, Y. and Wang, J. 2020. Modeling permanent strains of granular soil under cyclic loading with variable confining pressure. *Acta Geotechnica* 15(6), pp. 1409–1421. doi: 10.1007/s11440-019-00868-w.

Sun, X., Han, J., Kwon, J., Parsons, R.L. and Wayne, M.H. 2015. Radial stresses and resilient deformations of geogrid-stabilized unpaved roads under cyclic plate loading tests. *Geotextiles and Geomembranes* 43(5), pp. 440–449. doi: 10.1016/j.geotexmem.2015.04.018.

Tang, X., Stoffels, S.M. and Palomino, A.M. 2016. Mechanistic-empirical approach to characterizing permanent deformation of reinforced soft soil subgrade. *Geotextiles and Geomembranes* 44(3), pp. 429–441. doi: 10.1016/j.geotexmem.2015.06.004.

Tavakoli Mehrjardi, Gh. and Khazaei, M. 2017. Scale effect on the behaviour of geogrid-reinforced soil under repeated loads. *Geotextiles and Geomembranes* 45(6), pp. 603–615. doi: 10.1016/j.geotexmem.2017.08.002.

Wang, Z., Chen, Y., Xie, Y. and Xue, J. 2025. Investigation of geogrid-reinforced unbound granular material behavior using constant radial stiffness triaxial tests. *Geotextiles and Geomembranes* 53(3), pp. 728–743. doi: 10.1016/j.geotexmem.2025.01.007.

Zadehmohamad, M., Luo, N., Abu-Farsakh, M. and Voyiadjis, G. 2022. Evaluating long-term benefits of geosynthetics in flexible pavements built over weak subgrades by finite element and Mechanistic-Empirical analyses. *Geotextiles and Geomembranes* 50(3), pp. 455–469.